Evolution of Small-Scale Magnetic Elements in the Vicinity of Granular-Sized Swirl Convective Motions

**S. Vargas Domínguez · J. Palacios · L. Balmaceda ·
I. Cabello · V. Domingo**

Abstract Advances in solar instrumentation have led to widespread use of time series to study the dynamics of solar features, especially at small spatial scales and at very fast cadences. Physical processes at such scales are important as building blocks for many other processes occurring from the lower to the upper layers of the solar atmosphere and beyond, ultimately for understanding the larger picture of solar activity. Ground-based (*Swedish Solar Telescope*) and space-borne (*Hinode*) high-resolution solar data are analyzed in a quiet-Sun region that displays negative-polarity small-scale magnetic concentrations and a cluster of bright points observed in G-band. The region is characterized by two granular-sized convective vortex-type plasma motions, one of which appears to be affecting the dynamics of magnetic features and bright points in its vicinity and is therefore the main target of our investigations. We followed the evolution of the bright points, intensity variations at different atmospheric height, and the magnetic evolution for a set of interesting selected regions. We

S. Vargas Domínguez (✉)
Observatorio Astronómico Nacional, Universidad Nacional de Colombia, Bogotá, Colombia
e-mail: svargasd@unal.edu.co

J. Palacios · I. Cabello · V. Domingo
GACE, Image Processing Laboratory (IPL), Universidad de Valencia, P.O. Box 22085, 46071, Valencia,
Spain

Present address:
J. Palacios
Space Research Group-Space Weather, Departamento de Física y Matemáticas, Universidad de Alcalá,
28871 Alcalá de Henares, Madrid, Spain

L. Balmaceda · I. Cabello
ICATE/CONICET-UNSJ, CC 49, 5400 San Juan, Argentina

L. Balmaceda
INPE, P.O. Box 515, CEP 12227-010, Sao Jose dos Campos, Brazil

I. Cabello
Facultad Regional de Mendoza, Universidad Tecnológica Nacional, Mendoza, Argentina

ⓔ Springer

describe the evolution of the photospheric plasma motions in the region near the convective vortex and some plausible cases for convective collapse detected in Stokes profiles.

Keywords Sun: convection · Sun: granulation · Sun: photosphere · Sun: magnetic fields

1. Introduction

For many years, the spatial-resolution constraints in solar observations have prevented detailed observations of small-scale phenomena in the solar atmosphere. We are currently entering an era in which time series are widely used to study the dynamics of solar features at small spatial scales ($< 1''$) and at very rapid cadences (several images per minute). The study of multiple phenomena at such scales has proved to play a major role in understanding the physical processes that take place at different heights, from the lower to the upper layers of the solar atmosphere. Photospheric plasma motions are, in particular, of great interest as they directly affect the footpoints of magnetic loops rooted underneath the visible surface and generate deformations (*i.e.* stresses, twisting, and others) that might change the topology of the magnetic-field lines on their way up from the photosphere to the chromosphere and beyond. Recent observations suggest that a substantial part of the magnetic flux in quiet-Sun regions might be the result of the emergence of these small-scale and short-lived magnetic loops (see Martínez González and Bellot Rubio, 2009; Palacios *et al.*, 2012, and references therein) and that they can also contribute to heating of the solar chromosphere and corona (Wang *et al.*, 1995; Li *et al.*, 2007).

Convective processes take place as a mechanism of energy exchange involving plasma dynamics at different spatial and temporal scales. Small-scale convectively driven vortex-type motions have been discovered by Bonet *et al.* (2008) using high-resolution observations while tracking bright points (hereafter BPs) in the solar photosphere. Theory predicted these types of motions, but it is only recently, and thanks to highly resolved solar images, that these whirlpools have been detected. Moreover, these authors established logarithmic spiral trajectories followed by the BPs while the BPs were swallowed by a downdraft (*i.e.* sink). Vortex flows are commonly found in simulations at the vertices between multiple granules (Nordlund, 1986; Danilovic, Schüssler, and Solanki, 2010). Evidence of photospheric vortex flows has also been observed at larger scales (Brandt *et al.*, 1988) such as supergranular junctions (see also Attie, Innes, and Potts, 2009, and references therein). A recent study by Wedemeyer-Böhm and Rouppe van der Voort (2009) has revealed swirl events, featuring dark and bright fast-rotating patches in time series of chromospheric quiet-Sun regions inside coronal holes close to disk center. Although the motion of BPs seems to be connected to these swirl events, the actual physical link is yet to be found.

Danilovic, Schüssler, and Solanki (2010) observed strong downflows as precursors of the intensification of the magnetic field in the context of a convective collapse. In their simulations they found two out of three cases where vortices were formed related to magnetic-field intensifications at the junctions of granules. Some authors theorized that the turning motion of BPs leads to magnetic braiding and that the field lines can act as guide lines to spread waves from the photosphere to the chromosphere (Jess *et al.*, 2009; Goode *et al.*, 2010). For instance, Kitiashvili *et al.* (2011) simulated the turning motion and the subsequent appearance of waves. More recently, Wedemeyer-Böhm *et al.* (2012) proposed that such vortex motions can act as energy channels into higher layers in the solar atmosphere; they had compared multiwavelength observations and MHD simulations. The sizes of these events also vary depending on the spatial scale of the study. The size of the vortex was more than

7 Mm and persisted for several hours in the observations of Attie, Innes, and Potts (2009). Thus, these eddies were found in a variety of solar scales, from supergranular to medium-sized (Brandt *et al.*, 1988; Balmaceda *et al.*, 2010) and down to the smallest sizes that are detected and tracked using G-band bright points (Bonet *et al.*, 2008, 2010) with a size of 0.5 Mm. The smallest vortices from simulations were presented by Danilovic, Schüssler, and Solanki (2010), with a diameter of 0.2 Mm. The values for the vorticity are usually around 10^{-3} when related to observations (Bonet *et al.*, 2010; Vargas Domínguez *et al.*, 2011); however, simulations usually yield values of one or two orders of magnitude higher (*e.g.* Danilovic, Schüssler, and Solanki, 2010; Pandey and Wardle, 2012). Moll, Cameron, and Schüssler (2011) presented a simulation studying lifetimes, spatial coverages, and inclinations, and their dependence on divergence. Observations of vortical motions are not restricted to the vicinities of quiet-Sun BPs but they have also been observed in sunspots as rotating umbral dots (Bello González, Kneer, and Schlichenmaier, 2012) or even horizontal motions that may create lanes within granules (Steiner *et al.*, 2010).

In the present work we analyze a quiet-Sun region for which Balmaceda *et al.* (2010), hereafter BEA10, have reported a small-scale vortical motion that appears to affect the dynamic of magnetic concentrations. These authors reported on a vortex motion in the solar atmosphere associated with the rotation and "engulfment" of magnetic features as manifested by the analysis of solar magnetograms. The question arising from that work was whether the observed engulfment of small-scale magnetic elements by the vortex was the result of the stochastic evolution of granules or, perhaps, due to some interaction mechanism taking place underneath. In an attempt to unravel the problem described by BEA10, our main interest is the multiwavelength characterization of the region of interest (hereafter referred to as ROI) that is affected by the vortex (named V1). Intense activity of BPs (detected in G-band) is identified in the region, and these bright features are found to be affected by the swirling motion and their associated magnetic concentrations. We study the appearance of intergranular lanes and interpret their layouts as being ruled by the formation of vortex V1. Furthermore, we aim at describing the evolution of the photospheric plasma motions in the region as well as changes in the underlying magnetic field. We identify the formation of V1 in the computed flow maps and measure the variation of the mean velocity values for various stages in the evolution of the convective swirl event. We believe that these aspects (*i.e.* activity of BPs, magnetic concentrations, configuration of intergranular lanes, and photospheric plasma flows) are all intrinsically related, although the direct connections are yet to be found by adding more observational evidence and through numerical simulations that can accomplish these new scenarios. We have detected another convective vortex motion of similar size (named V2). The centers of divergence of the two swirls are separated by a distance of only 5″. This vortex, however, does not seem to influence the activity of BPs and small magnetic regions around it.

The article is structured as follows: Image acquisition and data processing are detailed in Section 2. In Section 3 we present a general description of the BPs, magnetic concentrations, and intergranular lanes in the region displaying the convective vortex motion. In Section 4 we focus on the photospheric plasma flows to show the formation and evolution of the vortex. In Section 5 we describe the behavior of small magnetic elements under the influence of the vortex motion. Section 6 is finally devoted to comments and a general discussion.

2. Observations and Data Preparation

The campaign performed at the *Swedish 1-m Solar Telescope* (SST: Scharmer *et al.*, 2003) was carried out during September – October 2007 as part of an international collaboration

Table 1 Characteristics of the time series acquired from ground-based and spacecraft facilities.

Telescope	Obs.	Series #	Time [UT]	Duration [minutes]	Number of images	Cadence [sec]	FOV [″]
SST	G-band	1	08:47 – 09:07	19	76	15	68.5 × 68.5
		2	09:14 – 09:46	32	128	15	68.5 × 68.5
Hinode	CN	1	08:40 – 09:20	40	70	35	19.2 × 74.1
	Ca II H	1	08:40 – 09:20	40	71	35	19.2 × 74.1
	Mg I	1	08:40 – 09:20	40	143	20	15.4 × 65.3
	SP	1	08:20 – 09:44	84	2558 scans	2	2.7 × 40.6

involving different institutions and researchers from Europe and Japan. This was a long campaign (24 days) with coordinated observations using not only the SST, but also three other solar telescopes: the *Dutch Open Telescope* (DOT), the *Vacuum Tower Telescope* (VTT), and the *Télescope Héliographique pour l'Etude du Magnétisme et des Instabilités Solaires* (THEMIS) at the Canary Islands Observatories in La Palma and Tenerife. The observations represented the first joint campaign that used all these ground-based solar facilities and the spacecraft mission *Hinode* (Kosugi *et al.*, 2007) in the framework of the *Hinode* Operation Program 14.

2.1. Ground-Based SST Data

The data from the SST that we analyzed were acquired during a particular observing run on 29 September 2007. The main target of interest was a quiet region close to the solar disk center ($\mu = 0.99$). Images in G-band ($\lambda 430.56$ nm) were recorded at a rapid cadence so that the multiframe blind-deconvolution (MFBD: Löfdahl, 1996, 2002) restoration technique could be applied to correct the data for atmospheric turbulence and instrumental aberrations, which degrade the quality of the images. CCD cameras with a size of $2048'' \times 2048''$ were employed and the effective field of view (hereafter FOV) corresponded to $68.5'' \times 68.5''$ with a sampling of $0.034''\,\mathrm{pix}^{-1}$. Only the best-quality images were preserved for further operations. Processing of the images included first the standard flat-fielding and dark-current subtraction, as well as the removal of hot and dark pixels and spurious borders in the flat-fielded images. After performing these steps, the images of the sequence were grouped in sets of about 125 frames acquired within time intervals of 15 seconds each. Every set yielded one restored image that almost reached the diffraction limit of the telescope ($\approx 0.1''$). Time series of restored images were finally corrected for diurnal field rotation, rigidly aligned, corrected for distortion, and subsonic filtered to eliminate *p*-modes and residual jittering (Title *et al.*, 1986). The final product was two time series (s1 and s2) of images (with a time gap of about seven minutes between them), as listed in Table 1 (SST).

2.2. *Hinode* Data

The data from *Hinode* on 29 September 2007 correspond to the coordinated observations previously described. The *Solar Optical Telescope* (SOT: Tsuneta *et al.*, 2008) onboard the *Hinode* spacecraft acquired filtergrams in the CN headband ($\lambda 388.35$ nm) and the core of Ca II H ($\lambda 396.85$ nm), with a cadence of ≈ 35 seconds and a pixel size of $0.054''$, using the *Broadband Filter Imager* (BFI). A subsonic-filtering procedure was finally applied to exclude high-frequency oscillations. The observed FOV corresponds to $19.18'' \times 74.09''$,
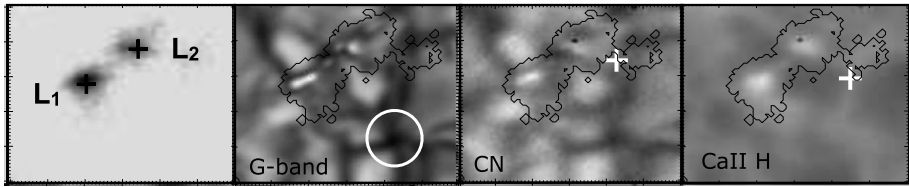
Figure 1 Sample of the observed region on 29 September 2007 at 08:48 UT (four-minute-average images) combining *Hinode* and SST (G-band) observations. From left to right: NFI magnetogram, G-band, CN, and Ca II H. The FOV is $\approx 6'' \times 5''$. L1 and L2 are the two main magnetic concentrations identified in the region. The white circle with 1 Mm diameter is centered on the location where a vortex motion is formed. Black contours outline the magnetic negative-polarity region. The FOV corresponds to the region studied in BEA10.

and almost the whole area of the *Hinode* FOV was covered by SST observations. Table 1 (*Hinode*) summarizes the parameters of the time series in more detail. The *Narrowband Filter Imager* (NFI) was employed to obtain magnetograms in the Mg I line ($\lambda 517.3$ nm) at a cadence of ≈ 20 seconds, with a pixel size of $0.08''$ and a FOV of $15.4'' \times 65.3''$. A sequence of images from the *Spectropolarimeter* (SP) instrument (Ichimoto *et al.*, 2008; Tsuneta *et al.*, 2008) was also acquired. This data set comprises the full Stokes I, Q, U, V parameters measured along a slit of 256 pixels in raster-scan mode of 18 scans during 08:20 – 09:44 UT, with a sampling of $0.15''$ pix^{-1} and a FOV of $2.66'' \times 40.57''$. A *dynamic mode* was used to allow studying extremely dynamic events by operating with an exposure time of 1.6 seconds per slit position. The noise level was $1.6 \times 10^{-3} I_c$ (where I_c is the continuum intensity) for Stokes I and $1.8 \times 10^{-3} I_c$ for Stokes Q and U. The SOT images were corrected for dark current, flat field, and cosmic rays by using the standard IDL SolarSoft routines. SP data were inverted using the LILIA inversion code (Socas Navarro, 2001), which is based on the SIR code (Ruiz Cobo and del Toro Iniesta, 1992). With this full atmosphere inversion code, several physical quantities were obtained, of which we used the magnetic-field strength, inclination, azimuth, and line-of-sight (LOS) velocity.

3. Description of the Quiet Sun in the Vicinity of the Vortex

Quasi-simultaneous data taken by *Hinode* and SST were used. Images were co-aligned and trimmed to obtain the same FOV in all wavelengths. We focused on a region with a considerable concentration of G-band bright points that are co-spatial with negative-polarity magnetic fragments. The magnetic patches are mostly distributed along a curved path with a larger negative core at one end. This is the region studied in BEA10, where those authors found a rotation of the magnetic concentration, as described above. The rotation is accompanied by small-scale processes of fragmentation and coalescence of BPs clearly discernible in G-band filtergrams, which take place along the intergranular lanes, as described in Section 5.

Two main magnetic concentrations (L1 and L2) are identified in BEA10; one of them rotates around the other. Figure 1 shows a sample of images taken at 08:48 UT. Every frame displays a four-minute average to enhance the features. The two magnetic concentrations are clearly discernible in the first frame in the figure. In Figure 2, we plot the trajectories followed by the magnetic centroid for L1 (plus-signs) and L2 (asterisks) calculated from the individual magnetic-strength maps obtained from SP data. Panels in the figure correspond to time intervals for G-band time series s1 and s2 (see Table 1), and arrows indicate the initial position for every trajectory and magnetic concentration, *i.e.* 08:47 UT for s1 and
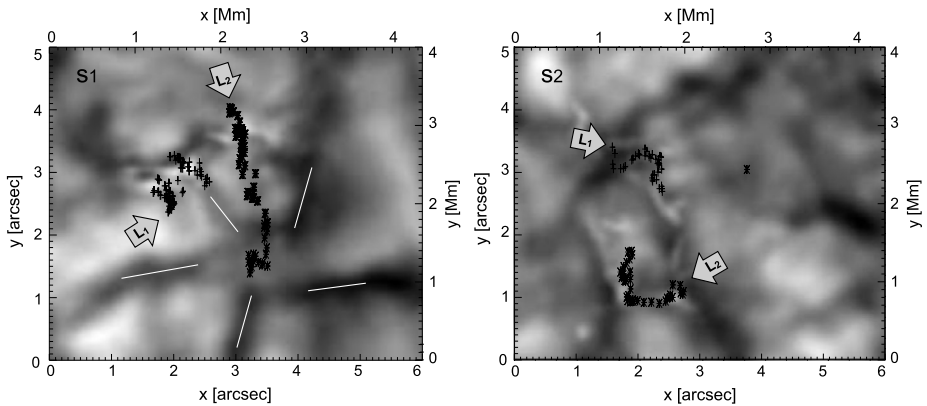
Figure 2 Evolution in time of the magnetic centroid for the two magnetic concentrations L1 and L2. Trajectories followed by the centroids are independently plotted for the SST/G-band series (s1/s2 for upper and lower panels). The arrows indicate the starting point for the L1 and L2 trajectories. Backgrounds are the corresponding time-average images in every case. White lines in the left panel outline the location of the intergranular lanes.

09:14 UT for s2. Trajectories are plotted overlaid on the average image in every case, *i.e.* 19 and 32 minutes for series s1 and s2. In Figure 2(s1) the locations of the centroid for L1 are confined in a smaller area than the L2 centroids, which drift noticeably toward the lower part of the FOV. Intergranular dark lanes are clearly seen in the average images, with widths of about 500 km. Straight white lines outline the mean location of the intergranular lanes that are found to be converging into a vertex in the granular pattern (referred to as the *draining point* in BEA10 and corresponding to the center of a convective vortex motion). Moreover, these white lines seem to be azimuthally equally spaced, forming an angle of $\approx 58 \pm 4$ degrees between two adjacent lines, except for the angle formed by the two lower right ones, which is wider. The white circle in Figure 1 is centered on the location where a vortex motion is formed during the corresponding time interval. The region is dominated by an intergranular lane (see arrow L1). The trajectory for L2 changes drastically from that in s1, and the converging intergranular lanes are not visible anymore. There are signs of bright points placed along many asterisks in L2. The configuration of the intergranular lanes and the evolution of the magnetic centroids in panels s1 and s2 in Figure 2 are proposed to be linked to a convective vortical motion. Panel s1 corresponds to the time of appearance of a vortical motion as detected in the plasma flow maps, whereas panel s2 reveals no hints of this type of motion, as we describe in detail in Section 6. Figure 3 plots the evolution in time of the magnetic centroid horizontal velocity magnitude (black) and the velocity in x (red) and y (green) directions as computed from the *Hinode*/SP data for L1 and L2. The centroid velocities were computed from the pairs of consecutive centroid positions for the respective magnetic concentration. For L2, we obtained that these horizontal velocities increase rapidly from ≈ 0.5 km s^{-1} up to ≈ 2 km s^{-1} during the time interval 08:40 – 09:07 UT, and then decrease. After that, the velocity increases again, reaching a second maximum of about 1.4 km s^{-1} at around 09:25 UT. L1 does not undergo significant motion. Horizontal velocities for L1 show a similar variation in magnitude during the first 30 minutes. Toward the end of the sequence, there is an increase in the velocity of up to 1.4 km s^{-1} while L1 is dragged by the surrounding flow.

Figure 3 Temporal evolution of horizontal velocities magnitude (black), velocity in *x* (red), and velocity in *y* (green) for the magnetic centroid as computed from the *Hinode*/SP data for L1 (upper panel) and L2 (lower panel). Times are in UT and velocities in km s^{-1}.
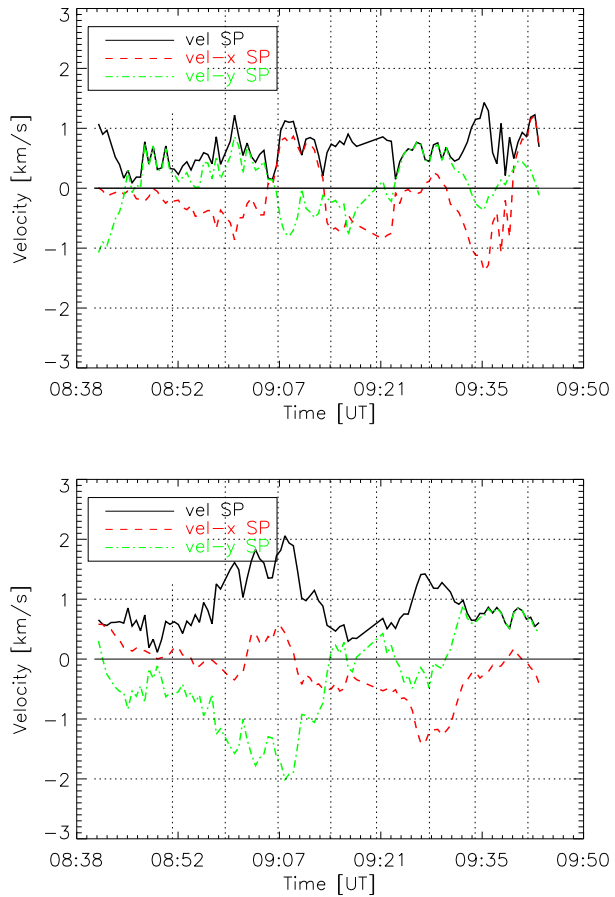
4. Photospheric Plasma Motions Associated with a Swirl Event

Solar plasma at the photospheric level displays a rapid evolution on the order of a few seconds. The high cadence of the acquired time series enables us to follow the evolution of the granulation pattern. In this section we aim to characterize the photospheric flows in the ROI that display the convective-swirl event. The SST/G-band and *Hinode*/CN time series were independently employed to compute the horizontal proper motions of structures by means of a local correlation-tracking (LCT) technique (November and Simon, 1988) implemented by Molowny-Horas and Yi (1994). Maps of horizontal velocities are calculated for time series s1 and s2 using a Gaussian tracking window with a FWHM of 1.0″. The size of the tracking window was selected after trying different values and finding an optimal one, *i.e.* not so small as to introduce noisy patterns, but large enough to detect even small vortices (note that the mean granular size is ≈ 1″). We applied the LCT analysis over a FOV of ≈ 10″ × 10″ that includes the ROI (of 6″ × 5″ shown in Figures 1 and 2). The flow maps computed from SST time series s1 are displayed in Figure 4, where the black box in the colored map represents the ROI FOV. The map in the upper-left panel is calculated by averaging over the total duration of the series (Δ*t* = 19 minutes). The underlying background represents the image of vertical velocities computed by multiplying the divergence of the
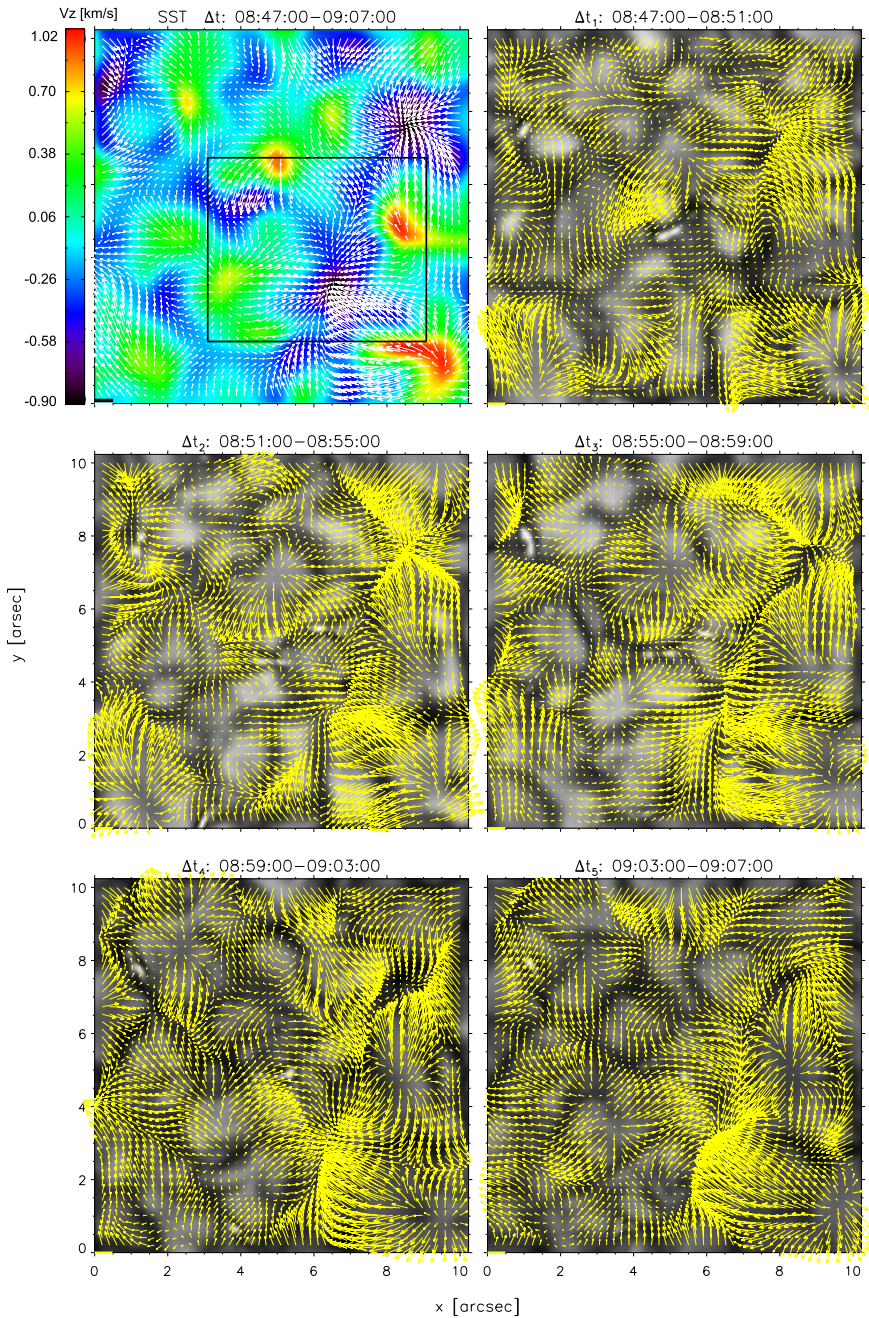
Figure 4 Horizontal velocities for different time intervals covering the G-band series s1. The upper-left map is computed for the whole duration of the series against the background of vertical velocities in false color. The ROI is framed in a black box with the same FOV ($6'' \times 5''$) as that in Figures 1 and 7. The other maps are computed over four-minute time intervals as labeled with background images displaying the corresponding average images. The length of the yellow horizontal bar at coordinates [0, 0] in every map corresponds to $1.5 \, \mathrm{km \, s^{-1}}$.

horizontal velocity field by a mass-flux scale-height factor described by November (1989). Flows coming from granular explosive events are dominant in the FOV and are normally associated with mesogranulation (Roudier and Muller, 2004; Bonet *et al.*, 2005). These events are clearly seen in the image of vertical velocities as strong positive magnitudes (upflows). We only identified two cases of strong sinks, *i.e.* negative vertical velocities with magnitude $\approx 0.9 \ \mathrm{km \ s^{-1}}$ (downflows), displaying converging horizontal flows (*i.e.* the velocity arrows point to a common destination) situated along intergranular lanes at coordinates [6.5, 3.5] and [8.5, 7.5], respectively. The first case corresponds to the main vortex V1 that we are interested in, which is located within the ROI studied in this work, and the second case, referred to as V2, is only briefly commented on in this section since it does not seem to affect the dynamics of the small magnetic elements in the region.

To study the evolution in time of this vortical motion, we applied the LCT again, but grouped the sequence in four-minute intervals from Δt_1 to Δt_5. The other panels in Figure 4 are the maps of horizontal velocities over the background representing the averaged four-minute images for every time interval. We first note an overall increment in the velocity magnitudes compared with the whole 19-minute flow map, as expected when averaging over shorter time intervals (November and Simon, 1988). Regarding the presence of the vortical motion in these map series, we found clear differences among them. Interval Δt_1 does not yet show a clear formation of the vortex (*i.e.* increase in vorticity), but a faint sign of its developing phase, and only for Δt_2 do we start to observe some of the features seen in the map averaged over the whole time sequence Δt, although the central point of convergence appears elongated in the vertical direction. At the time of this second interval, the vortex V2 in particular is very well formed and consistently recognizable in the upper-right region of the FOV as an X-shaped structure. In the next three intervals (Δt_3, Δt_4, and Δt_5) we found evidence of a clear appearance of vorticity, and the vortex is more symmetrical at interval Δt_4. In particular, for the interval Δt_4, some flows appear to be *falling* into the *draining point* from an upper location along trajectories resembling the ones followed by the BPs described in Section 3 that are probably responsible for their observed behavior (referred to as "engulfment" in BEA10).

To establish a value for the lifetime of the vortex, the LCT was extended to later temporal intervals by using the second time series (series s2 in SST, Table 1). Unfortunately, we have a six-minute gap where there are no data available. The map of horizontal proper motions averaged over the whole duration of s2 (32 minutes) is displayed in the top left panel in Figure 5 with the background again representing the computed vertical velocities (note that the scale is not the same as in Figure 4 since the averages are computed over time series of different durations, *i.e.* 19 and 32 minutes, as mentioned above). The black box extracts the same ROI as in the upper-left panel in Figure 4. The once-strong sink (and vortex) in the analysis of series s1 has turned into a smoother structure with downward velocity magnitudes of only a few km per second in magnitude ($\approx 2 \ \mathrm{km \ s^{-1}}$) in our velocity scale. In an attempt to identify whether the vortex has completely disappeared for shorter time averages, we pursued the same procedure as before by averaging over four-minute intervals. The flow maps in Figure 5 display no signatures of this steady photospheric vortex-type flow. Only for the first four-minute average map is there a small sign of what could be the remaining of a diluted vortex shifted to the left by ≈ 1 arcsec as pushed away by strong velocities starting to develop in the lower right part of the FOV in the last panel in Figure 4. According to this analysis, we estimate the lifetime of the vortex to be of at least ≈ 15 minutes, as detected from the flow map starting at 08:51 UT to the one ending at 09:07 UT. These values are higher than the $\approx$ five-minute lifetime of the vortex-type motions described by, *e.g.*, Bonet *et al.* (2008) but, in contrast to the calculation of these authors, we have not
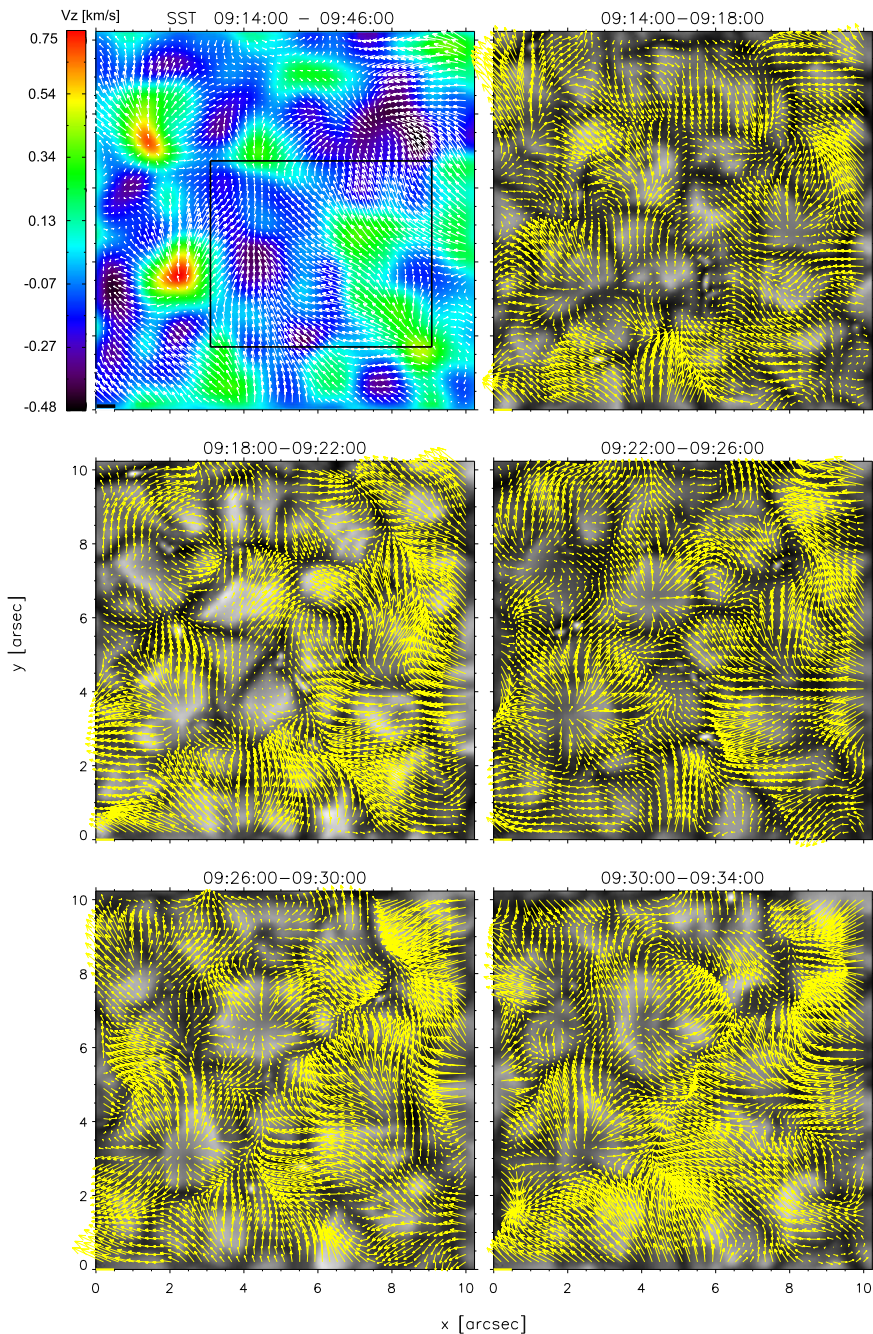
Figure 5 Horizontal velocities for different time intervals covering the G-band series s2. The upper-left map is computed for the whole duration of the series against the background of vertical velocities in false color. The other maps are computed over four-minute time intervals as labeled with background images displaying the corresponding average images. The length of the yellow horizontal bar at coordinates [0, 0] in every map corresponds to 1.5 km s^{-1}. Note that the scale for vertical velocities differs from that in Figure 4 because of the different duration of the time series, which affects the velocity averages. See text for details.
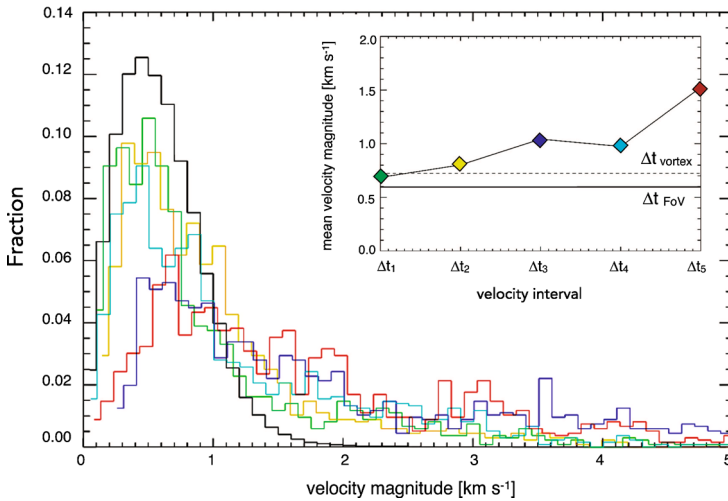
Figure 6 Histogram of horizontal velocities computed for different time intervals for the G-band time series s1, $\Delta t = 19$ minutes (black) and four-minute interval averages Δt_1 (green), Δt_2 (yellow), Δt_3 (blue), Δt_4 (cyan), and Δt_5 (red). Statistics of velocities are computed in a region including the vortex. The upper panel plots the mean velocity magnitudes in the histogram for the different intervals, where Δt_{vortex} (horizontal dotted line) and Δt_{FOV} (horizontal black line) represent the mean velocity computed in the box framing the vortex and in the whole FOV in the top left panel in Figure 4, respectively (see text for details).

estimated it depending on the evolution of BPs in the region, but from the proper motions of convective plasma.

The statistics of the horizontal velocities are computed for all of the time intervals (Δt and Δt_1 to Δt_5). Figure 6 plots the histograms where the black curve represents the one for Δt and the color histograms correspond to the four-minute interval averages. The velocity statistics are computed in a region including the vortex by establishing a threshold in the divergence field to mask the vortex area coverage, thus computing the vectors in the nearest vicinity to the center of convergence. The small upper panel in the figure plots the mean velocity magnitude for the four-minute intervals as colored diamonds (same colors as used for histograms) in the same vortex areas. The horizontal dotted line (Δt_{vortex}) represents the value for the mean velocity magnitude as computed from the whole time interval [Δt] in the black box framing the vortex (see top left panel in Figure 4), and the horizontal black line [Δt_{FOV}] accounts for the same value in the whole FOV ($\approx 10'' \times 10''$). There is a clearly increasing trend for the mean velocity magnitudes when moving in time from Δt_1 to Δt_5, starting from a value of ≈ 0.7 km s^{-1} (Δt_1) very close to the mean velocity magnitude averaged over the whole FOV (Δt_{vortex}; when the vortex has not yet been formed). A period of stability (of about ten minutes) in the velocity magnitude is registered for Δt_3 and Δt_4 corresponding to steady-vortex flows in the maps in Figure 4. After that, for interval Δt_5, we find evidence of large flows coming from fast flows due to exploding granules taking place in the lower right corner of the FOV.

Although our studied vortex seems to have disappeared in the flow maps for s2, the other important sink in the FOV hosting vortex V2 remains present and in a developed stage. The evolution of V2 can be followed throughout the flow maps in Figures 4 and 5 at [8, 7.5]. The vortical motion appears to be more stable and lasts longer but has a similar spatial coverage. Surprisingly, this vortex does not seem to affect the dynamics of BPs in their vicinity in the G-band time sequence. Concerning *Hinode* data, the map of horizontal velocities was
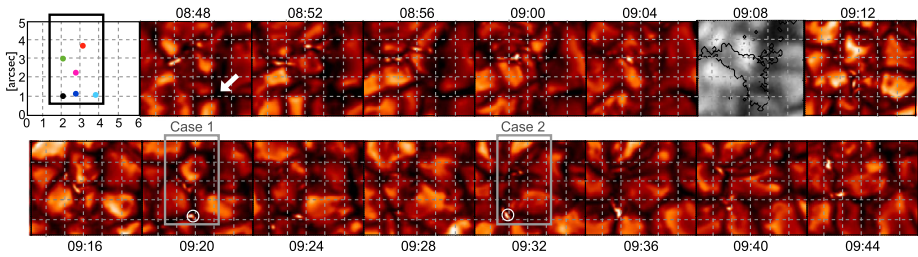
Figure 7 Sequence of contrasted SST/G-band images for both time series s1 and s2 showing the evolution of the studied quiet-Sun region on 29 September 2007. Frame at 09:08 UT (in gray-scale) corresponds to a *Hinode*/CN image that covers the gap between s1 and s2 during the SST observation, with black contours outlining the negative magnetic polarity area. These frames display the average image over four-minute intervals and the time stamps correspond to the initial time. The top-left frame shows the location of five regions of interest (colored dots). The white arrow in frame at 08:48 pointing to the center of a convective vortex motion detected in the FOV is included for reference. Boxes in black (top sequence) and gray (bottom sequence) extract a common FOV. Case 1 (at 09:20) and Case 2 (at 09:32) stand for the analysis of plausible convective collapse events shown in Figure 9. The locations displaying an intensification of BPs are encircled in white.

computed over the CN sequence (not shown in the article) and the results are similar to those described above for SST/G-band data, although the noise increases due to the lower spatial resolution.

5. Activity of Small Magnetic Elements

The quiet-Sun region studied is populated by BPs associated with the magnetic concentrations, as remarked in previous sections. The activity of BPs reveals intrinsic properties of the intense magnetic fields that emerge from the solar interior at such small spatial scales (*e.g.* Ishikawa *et al.*, 2007). Using the high-resolution G-band time series, we can identify the rapid evolution of the region, *i.e.* exploding granules, reorganization of the granular pattern, and a population of BPs. Figure 7 displays the sequence of images of the ROI (including the two SST/G-band time series s1 and s2 in false color, separated by the gray-scaled *Hinode*/CN image at 09:12 UT). The white arrow is a reference pointing to the location of the swirl convective motion that develops in the region. Single BPs and chains of BPs are highly dynamic, and we can show clear stages of fragmentation (*i.e.* 08:48 – 09:00 UT) and coalescence (09:05 – 09:20 UT) accompanied by spatial displacements and intensity changes.

The intensity variations in the series of CN, Ca II H, G-band, and magnetograms are computed in a small box ($7'' \times 7''$) at selected points (colored dots in first panel in Figure 7. Figure 8 plots the variation in time of intensity for two of the selected locations (black and blue dots) in the vortex's nearest vicinity. Although special attention is drawn to the magnetic-field intensifications occurring after 09:20 UT that are described in the next section, we include their intensity profiles for the whole time interval. From the analysis of these profiles together with visual exploration of Figure 7 we can infer that the region undergoes significant changes due to the vortex motions in the early phase. Later on, important peaks in G-band intensity are seen at around 09:20 – 09:25 (black curve) and 09:32 – 09:40 (blue curve). Peaks in the intensity profiles are associated to the formation of BPs product of coalescence processes, and they accompany changes in the underlying magnetic field as a consequence of V1 described in the previous section. The magnetic activity and average intensity in some locations are strongly linked to the rotation of the magnetic structures that
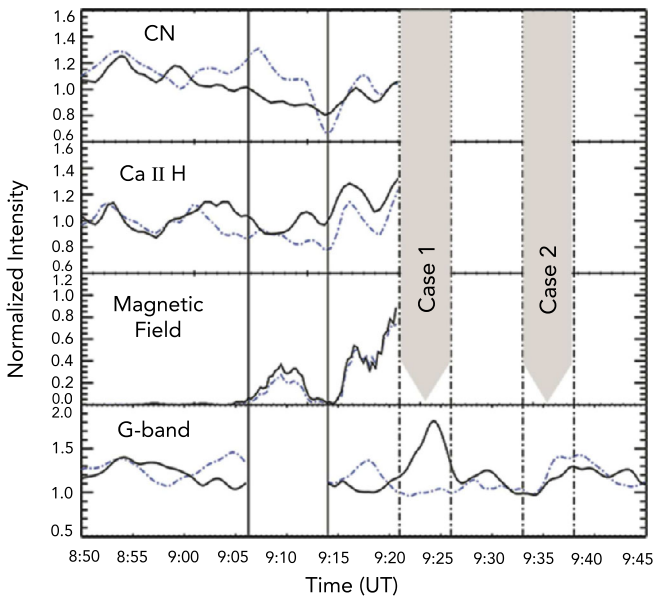
Figure 8 Normalized intensity profiles for selected locations in different series of images. First three rows (from top to bottom) from the analysis of *Hinode*/BFI (CN and Ca II H) and NFI (magnetic field in Mg I) data, and the last row from SST data. The vertical solid lines separate the two time series s1 and s2 in SST/G-band data with the seven-minute gap in between. Dot–dashed blue and black curves correspond to the locations of corresponding colored dots in the top-left panel in Figure 7. The two vertical shadowed areas highlight the time periods of the plausible convective collapse events (cases 1 and 2) analyzed in Figure 9 that correspond to the location of the dark-blue and black dots in the first panel in Figure 7 and encircled in white in the same figure.

seems to be dragged by the vortex developed during the time coverage of s1. Some of the flows in Figure 4 are precisely observed within the ROI along trajectories connecting BPs and ending up in the region where the center of the vortex is located, and hence bringing plasma and embedded magnetic elements together to the vortex.

5.1. Magnetic-Field Intensification

Using *Hinode*/SP data, we analyze two particular cases for plausible convective collapses taking place close to the vortex region. Magnetic-field magnification/intensification is observed soon after the vortex has disappeared. Figure 9 shows: i) Stokes-V profiles of the magnetically sensitive 630.1 nm and 630.2 nm Fe I lines, ii) maps displaying LOS velocities (V_{LOS}) obtained by Dopplershift calculation on Stokes I, and iii) co-temporal magnetograms in absolute value $[|V|/\langle I_c \rangle]$ obtained from the peak Stokes V. The two cases are referred to as cases 1 and 2. In case 1 (see row labeled A in Figure 9) maps are displayed every 36 seconds while Stokes-V profiles are plotted every 72 seconds (*i.e.*, every two maps) measured at the center of the region encircled in white in the maps (at 09:22 UT). A green crosshair pinpoints the area where these profiles are obtained. Asymmetries between the two magnetic concentrations are evident. In the fourth panel in row A, a three-lobed profile appears in the 630.1 nm but not in the 630.2 nm line, suggesting the presence of stronger gradients (of magnetic field strength or velocity) above the lower photosphere (630.1 nm line). This could be due to sub-resolution overlapping Stokes-V profiles; see for
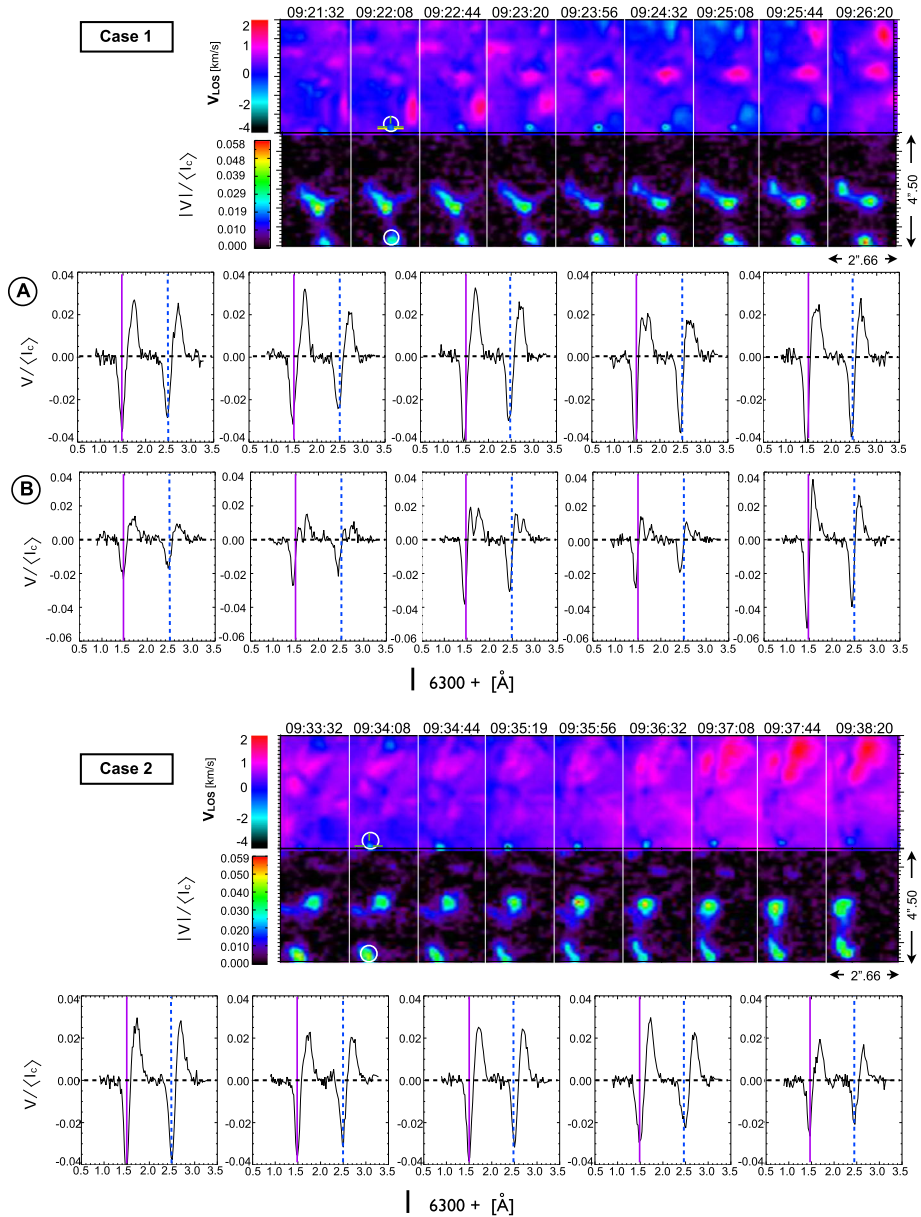
Figure 9 Detected cases of plausible convective-collapse events in *Hinode* data on 29 September 2007. For every case the temporal sequence of LOS Doppler velocities (upper row) and magnetic signal (lower row) are simultaneously shown in false-color maps. Encircled in white are regions displaying redshifts accompanied by an intensification in the magnetic field. Stokes-*V* profiles are correspondingly plotted for these regions (from the subpanel holding the white circumference to the following four panels), along with magenta and blue lines indicating the nominal wavelengths.

instance Socas-Navarro and Manso Sainz (2005) and references in Palacios *et al.* (2012). This phenomenon occurs during the period 09:22 – 09:25 UT, when the peak LOS velocity is about -3.5 km s^{-1}. The sequence in row B (case 1) in the same figure shows Stokes-V profiles for an adjacent pixel, highlighted in yellow by a crosshair. Again, the appearance of three-lobed Stokes-V profiles may indicate gradients of velocity. In the fourth panel, a sudden appearance of a more-symmetric profile suggests a stabilization of the magnetic field or velocity gradients of the associated BP. In the G-band filtergrams, the new BPs associated with this event are observed in this region (see encircled region in the frame at 09:20 UT in Figure 7). For case 2, the symmetric profiles calculated for the encircled region in the corresponding maps at 09:34 and the pixel marked by a green crosshair do not suggest strong changes on gradients, and the magnetic region is rather stable in time. However, during an interval of 72 seconds from 09:33:32 to 09:34:44 UT), we observe a variation in velocity from -1.0 to -3.5 km s^{-1}. Similar to case 1, BPs appear in this location in the G-band images (encircled in white at 09:34) simultaneously with the convective collapse event and lasting for about eight minutes.

Velocities in the magnetized atmosphere can be estimated from a zero-crossing Stokes-V. We can perform a rough guess of the velocity values from the Stokes-V profiles and their nominal wavelengths, marked with magenta for the 630.1 nm and blue for the 630.2 nm line. We estimate the wavelength shifts to be about $0.01 - 0.015$ nm, which leads to downflow velocities in the range of -4.7 to -7.1 km s^{-1}. Therefore, another key element of the convective collapse, the supersonic downflow, comes into play. Both cases extend over an area of about $4 - 6$ pixels ($0.30'' \times 0.30''$) and have lifetimes of about five to eight minutes. Asymmetric profiles and downflows have been found and explained in different works, *e.g.* Orozco Suárez *et al.* (2008), Fischer *et al.* (2009). Bello González *et al.* (2009) also found asymmetric Stokes-V profiles where a BP also showed flux intensification and downflows. For completeness of this case, we also inspected the magnetic-field strength and LOS-velocity maps for the time interval from 09:20 to 09:40 UT. The magnetic-field strength was retrieved with the inversion code LILIA. The atmospheric model is a one-component full atmosphere, from $\log(\tau) = -6$ to $\log(\tau) = 1.4$, considering LTE and hydrostatic equilibrium. The optical depth chosen is $\log(\tau) = -1$. The filling factor is not a free parameter. LOS velocity maps, on the other hand, were obtained by estimating the Doppler shift of the nominal wavelength center with the center-of-gravity method from the Stokes-I. For more details, we refer to Balmaceda *et al.* (2010).

In Figure 10, we plot the maximum magnetic-field strength [B] and the maximum redshifted velocity for the southernmost magnetic structure (inside the white circumferences in Figure 9). These plots show strong downflows (on the order of -3 km s^{-1}) accompanied by some field intensification, which are not significant, however, and which took place some minutes after the peak in velocity. These peaks can also be related to the intensification of the G-band intensity (bottom panel in Figure 8). The peak in the G-band intensity at 09:24 on the BP marked in black may correspond to the first strong downflow (case 1). The small peak in the G-band intensity around 09:30 may be related to the highest value of B. The intensification after the second downflow after 09:33 (case 2) shows an increasing trend similar to that of the G-band intensity. We chose to plot the magnetic strength instead of the flux density because SP was in a dynamic mode, and noise may be high in Q and U.

The small variation of the field strength observed here can be explained as due to subresolution flux tubes or even counterflows in the tube that may cause an incomplete convective collapse (Bellot *et al.*, 2001; Socas-Navarro and Manso Sainz, 2005). The magnitude of the observed field intensification and downflow velocities, however, agrees with the first phase of the event described by, *e.g.*, Bellot *et al.* (2001).
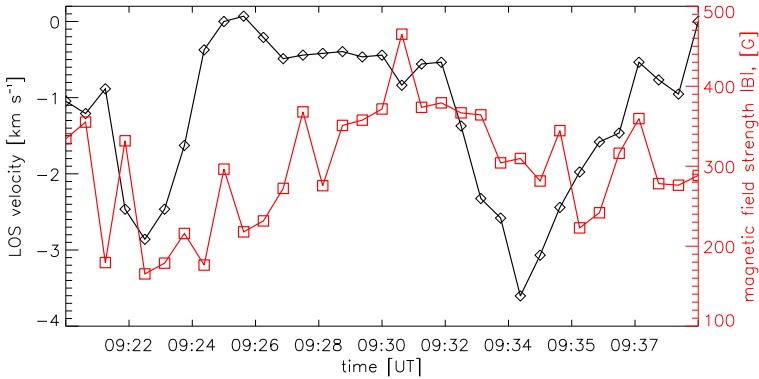
Figure 10 Evolution of peak magnetic-field strength [$|B|$, red squares] and maximum redshifted LOS velocity (black diamonds) for case 1 (from $\approx 09:21$ to 09:27 UT) and case 2 (from 09:33 to 09:38 UT) in the regions encircled in white in Figure 9. Note that the bright point that corresponds to case 1 is already visible at the leftmost part of the plot. Two important downflows at 09:21 and 09:33 UT and a peak in the magnetic field at 09:30 UT are displayed (see text for details).

6. Discussion

We presented a continuation of the work in BEA10, who reported the observation of magnetic concentrations dragged into a convective vortex motion in the photosphere. We furthermore studied the ROI ($10'' \times 10''$) and analyzed the two examples of convective vortical motions referred to as V1 and V2 (each one affecting a circular area of radius $\approx 3.0''$ from the vortex center), with V2 lasting for more than an hour. The stability and lifetime of vortical motions are strongly linked to the evolution of the granular pattern, and they seem to gather larger velocity magnitudes in their more developed stage. BEA10 reported small-scale magnetic concentrations of negative polarity affected by one of these convective swirl motions of plasma and identified two main magnetic concentrations of which one does not seem to be affected and remains rather stationary, while the other magnetic concentration is dragged and approaches the center of vortex V1. In our analysis of the same region we determined the motion of the magnetic centroid for each of these magnetic concentrations and showed that one of them is affected as long as the vortex is present. The configuration of the intergranular lanes with an azimuthally quasi-symmetric distribution as seen in the average image and the evolution of the magnetic centroids are proposed to be linked to a convective vortical motion. The vortical motion has different developing stages, as shown by the computed horizontal flow maps, which record a more stable period that lasts for about ten minutes. The onset of V1 is characterized by rather low mean velocity magnitudes (600 m s^{-1}), and the value increases up to 1 km s^{-1} while reaching the period of stability mentioned above. The fate of V1 seems to be determined by strong flows coming from the lower left part of the FOV that sweep away the coherence of the vortical motions and increase the mean velocity value to about 1.5 km s^{-1}. We estimated the lifetime of V1 to be ≈ 15 minutes. The configuration of the region in terms of horizontal flows, after V1 has disappeared, resembles that for a mesogranular flow pattern (see for instance the lower panels in Figure 5). Bonet *et al.* (2008) found that BPs describe spiral trajectories toward the center of convectively driven vortex flows, although these authors did not claim to observe fragmentation or coalescence processes associated with the activity of the visually tracked BPs. In our analysis we found intense activity of BPs, including fragmentation and intensification due to coalescence at the time when the magnetic concentrations rotate and seem

to be dragged by the formation of the convective vortex motion (08:48 to 09:08 UT in the sequence in Figure 7). The comparison with the activity of BPs in regions isolated from the effects of convective vortex motions is beyond the scope of the present work, but we acknowledge that it should be properly addressed to determine the complete influence of these types of motions in shaping the granular patterns at fine spatial scales.

In the cases presented in Figure 9, small magnetic patches experience a sudden strong downflow and some intensification of the magnetic-field strength. Since magnetic elements are present in the locations before the event (*i.e.* the strong downflow appearance), these cases are likely convective collapses of a part of the magnetic area or a flux intensification, and can be explained as unstable flux tubes with high field strength (Spruit, 1979). Nagata *et al.* (2008) showed cases of high-speed downflow intensifications of the magnetic field and the appearance of BP. According to Bellot *et al.* (2001), the process of flux concentration is connected with strong redshifts, while the destruction of a magnetic structure is associated with high blueshifts. Narayan (2011) reported that the increasing velocities in downflows correspond to a magnetic-field intensification. These cases are interesting, since they can provide an observational counterpart to the simulations of Danilovic, Schüssler, and Solanki (2010), for instance. These events of strong downflows within the magnetic structures and moderate intensification might be driven by the strong horizontal flow from the nearby exploding granule on the right. L2 presents a peak in the horizontal velocity at 09:28 UT that could be related to the magnetic-field intensifications. In addition to the studied vortex [V1], there is another vortex (V2) in our region of interest that is very stable and lasts for at least 40 minutes. An interesting fact is that the BPs detected at the beginning of the time series are closer in space to V2 than to the vortex that drags the magnetic concentrations. Magnetic elements seem to be unaffected by V2. To understand this scenario, we would have to determine how the flux tubes associated with the BPs are rooted and ascertain possible connections and interactions that might be influenced by the convective flows below the photospheric level. According to our observational evidence, the small-scale flux tubes may be deformed underneath the optical surface with a region closer to the vortex that seems to affect them, but they could be located closer to the other vortex (V2 in our studied example) at the photosphere.

The evolution of photospheric flows at different spatial scales might initiate solar activity in the upper layers by triggering reconnection and propagation of waves, among others, *e.g.* supergranular flows, as reported by Innes *et al.* (2008). Small-scale vortical motions on the solar photosphere are therefore thought to play an important role in the dynamics of the quiet Sun (van Ballegooijen *et al.*, 1998; Kitiashvili *et al.*, 2011), not only by merging magnetic concentrations and thus forming more stable structures (*e.g.* pores), but also by promoting displacement of footpoints associated with small magnetic loops that connect the surface and the upper chromospheric layer, hence allowing reconnection to take place when opposite-polarity magnetic fields are present.

According to simulations, photospheric vortical motions contribute to merging of small magnetic concentrations, *i.e.* the magnetic field is advected by the flow, as remarked above, and this is plausible because the mechanism responsible for the formation and evolution of stronger magnetic concentrations and ultimately pores, accompanied by strong downflows down to a distance of a few Mm beneath the visible solar surface. The analysis of plasma motions around solar pores shows that their nearest vicinity is dominated by both inflows (Vargas Domínguez, 2008; Vargas Domínguez *et al.*, 2010) and signs of downflows (Hirzberger, 2003). More observational evidence should be studied to clarify the real connection and the acting part of convective vortex flows in this context. In our studied region there are only negative-polarity elements, but there is also some evidence (Kubo, Low, and

Lites, 2010) claiming the cancellation of opposite-polarity magnetic elements as approaching a junction of intergranular lanes in regions displaying converging horizontal flows.

Converging and downward motions have therefore proved to be important in bringing together magnetic elements either with the same or with opposite polarities and changing the topology of small low-lying loops in the solar surface. Convective vortex-type motions should be considered to determine the way that they affect the evolution of magnetic elements from the photosphere to upper layers; therefore the observational findings presented are important in adding new evidence on the dynamics of small-scale structures in the solar photosphere.

References

Attie, R., Innes, D.E., Potts, H.E.: 2009, *Astron. Astrophys.* **493**, L13.

Balmaceda, L., Vargas Domínguez, S., Palacios, J., Cabello, I., Domingo, V.: 2010, *Astron. Astrophys.* **513**, L6.

Bello González, N., Kneer, F., Schlichenmaier, R.: 2012, *Astron. Astrophys.* **538**, 62.

Bello González, N., Yelles Chaouche, L., Okunev, O., Kneer, F.: 2009, *Astron. Astrophys.* **494**, 1091.

Bellot, L., Rodriguez Hidalgo, I., Collados, M., Khomenko, E., Ruiz Cobo, B.: 2001, *Astrophys. J.* **560**, 1010.

Bonet, J.A., Márquez, I., Muller, R., Sobotka, M., Roudier, Th.: 2005, *Astron. Astrophys.* **430**, 1089.

Bonet, J.A., Márquez, I., Sánchez Almeida, J., Cabello, I., Domingo, V.: 2008, *Astrophys. J. Lett.* **687**, L13.

Bonet, J.A., Márquez, I., Sánchez Almeida, J., Palacios, J., Martínez Pillet, V., Solanki, S.K., del Toro Iniesta, J.C., Domingo, V., Berkefeld, T., Schmidt, W.: 2010, *Astrophys. J. Lett.* **723**(2), L139.

Brandt, P.N., Scharmer, G.B., Ferguson, S., Shine, R.A., Tarbell, T.D.: 1988, *Nature* **335**, 238.

Danilovic, S., Schüssler, M., Solanki, S.K.: 2010, *Astron. Astrophys.* **509**, A76.

Fischer, C.R., de Wijin, A.G., Centeno, R., Lites, B.W., Keller, C.U.: 2009, *Astron. Astrophys.* **504**, 583.

Goode, P.R., Yurchyshyn, V., Cao, W., Abramenko, V., Andic, A., Ahn, K., Chae, J.: 2010, *Astrophys. J. Lett.* **714**(1), L31.

Hirzberger, J.: 2003, *Astron. Astrophys.* **405**, 331.

Ichimoto, K., Lites, B., Elmore, D., Suematsu, Y., Tsuneta, S., Katsukawa, Y., *et al.*: 2008, *Solar Phys.* **249**, 233. ADS. DOI.

Innes, D.E., Genetelli, A., Attie, R., Potts, H.E.: 2008, In: *12th European Solar Physics Meeting*, Freiburg, 2.86. ADS, http://espm.kis.uni-freiburg.de/fileadmin/user_upload/espm/Proceedings-Talks/t_2.3-09.pdf.

Ishikawa, R., Tsuneta, S., Kitakoshi, Y., Katsukawa, Y., Bonet, J.A., Vargas Domínguez, S., Rouppe van der Voort, L.H.M., Sakamoto, Y., Ebisuzaki, T.: 2007, *Astron. Astrophys.* **472**, 911.

Jess, D.B., Mathioudakis, M., Erdélyi, R., Crockett, P.J., Keenan, F.P., Christian, D.J.: 2009, *Science* **323**, 1582.

Kitiashvili, I.N., Kosovichev, A.G., Wray, A.A., Mansour, N.N.: 2011, *Astrophys. J. Lett.* **727**, L50.

Kosugi, T., Matsukaki, K., Sakao, T., Shimizu, T., Sone, Y., Tachikawa, S., *et al.*: 2007, *Solar Phys.* **243**, 3. ADS. DOI.

Kubo, M., Low, B.C., Lites, B.W.: 2010, *Astrophys. J.* **712**, 1321.

Li, H., Sakurai, T., Ichimito, K., Suematsu, Y., Tsuneta, S., Katsukawa, Y., Shimizu, T., Shine, R.A., Tarbell, T.D., Title, A.M., *et al.*: 2007, *Publ. Astron. Soc. Japan* **59**, S643.

Löfdahl, M.G.: 1996, Ph.D. Thesis, Stockholm Univ.

Löfdahl, M.G.: 2002, *Proc. SPIE* **4792**, 146.

Martínez González, M.J., Bellot Rubio, L.R.: 2009, *Astrophys. J.* **700**, 1391.

Molowny-Horas, R., Yi, Z.: 1994, ITA (Oslo) Internal Rep. No. 31s.

Moll, R., Cameron, R.H., Schüssler, M.: 2011, *Astron. Astrophys.* **533**, A126.

Nagata, S., Tsuneta, S., Suematsu, Y., Ichimoto, K., Katsukawa, Y., Shimizu T., Yokoyama, T., Tarbell, T.D., Lites, B.W., Shine, R.A., Berger, T.E., Title, A.M., Bellot Rubio, L.R., Orozco Suárez, D.: 2008, *Astrophys. J. Lett.* **677**, L145.

Narayan, G.: 2011, *Astron. Astrophys.* **529**, A79.

Nordlund, Å: 1986, In: Deinzer, W., Knölker, M., Voigt, H.H. (eds.) *Small Scale Magnetic Flux Concentrations in the Solar Photosphere*, Vandenhoeck & Ruprecht, Göttingen, 83.

November, L.J.: 1989, *Astrophys. J.* **344**, 494.

November, L.J., Simon, G.W.: 1988, *Astrophys. J.* **333**, 427.

Orozco Suárez, D., Bellot Rubio, L.R., del Toro Iniesta, J.C., Tsuneta, S.: 2008, *Astron. Astrophys.* **481**, L33.

Palacios, J., Balmaceda, L.A., Vargas Domínguez, S., Cabello, I., Domingo, V.: 2012, In: Sekii, T., Watanabe, T., Sakurai, T. (eds.) *Hinode-3: The 3rd Hinode Science Meeting* **CS-454**, Astron. Soc. Pac., San Francisco, 51.

Pandey, B.P., Wardle, M.: 2012, *Mon. Not. Roy. Astron. Soc.* **426**, 1436.

Roudier, Th., Muller, R.: 2004, *Astron. Astrophys.* **419**, 757.

Ruiz Cobo, B., del Toro Iniesta, J.C.: 1992, *Astrophys. J.* **398**, 375.

Scharmer, G.B., Bjelksjö, K., Korhonen, T.K., Lindberg, B., Petterson, B.: 2003, *Proc. SPIE* **4853**, 341.

Socas Navarro, H.: 2001, In: Sigwarth, M. (ed.) *Advanced Solar Polarimetry – Theory, Observation, and Instrumentation* **CS-236**, Astron. Soc. Pac., San Francisco, 487.

Socas-Navarro, H., Manso Sainz, R.: 2005, *Astrophys. J. Lett.* **620**, L71.

Spruit, H.C.: 1979, *Solar Phys.* **61**, 363. ADS, DOI.

Steiner, O., Franz, M., Bello González, N., Nutto, Ch., Rezaei, R., Martínez Pillet, V., Bonet Navarro, J.A., del Toro Iniesta, J.C., Domingo, V., Solanki, S.K., Knölker, M., Schmidt, W., Barthol, P., Gandorfer, A.: 2010, *Astrophys. J. Lett.* **723**, L180.

Title, A.M., Tarbell, T.D., Simon, G., the SOUP team: 1986, *Adv. Space Res.* **6**, 253.

Tsuneta, S., Ichimoto, K., Katsukawa, Y., Nagata, S., Otsubo, M., Shimizu, T., *et al.*: 2008, *Solar Phys.* **249**, 167. ADS, DOI.

van Ballegooijen, A.A., Ninenson, P., Noyes, R.W., Löfdahl, M.G., Stein, R.F., Norlund, Å, Krishnakumar, V.: 1998, *Astrophys. J.* **509**(1), 435.

Vargas Domínguez, S.: 2008, PhD thesis, Univ. La Laguna.

Vargas Domínguez, S., de Vicente, A., Bonet, J., Martínez Pillet, V.: 2010, *Astron. Astrophys.* **516**, 91.

Vargas Domínguez, S., Palacios, J., Balmaceda, L., Cabello, I., Domingo, V.: 2011, *Mon. Not. Roy. Astron. Soc.* **416**, 148.

Wang, Y., Noyes, R.W., Tarbell, T.D., Title, A.M.: 1995, *Astrophys. J.* **447**, 419.

Wedemeyer-Böhm, S., Rouppe van der Voort, L.: 2009, *Astron. Astrophys.* **507**, L9.

Wedemeyer-Böhm, S., Scullion, E., Steiner, O., Rouppe van der Voort, L., de La Cruz Rodríguez, J., Fedun, V., Erdélyi, R.: 2012, *Nature* **486**, 505.